Applied Clay Science 213 (2021) 106265

Contents lists available at ScienceDirect

Applied Clay Science

journal homepage: www.elsevier.com/locate/clay

Conductive halloysite clay nanotubes for high performance sodium ion battery cathode

Xiang Cao [a,1], Yingjuan Sun [a,1], Yongrong Sun [b], Dong Xie [b], Hongyan Li [a,*], Mingxian Liu [a,*]

[a] Department of Materials Science and Engineering, Jinan University, Guangzhou 510632, China
[b] Institute of Bioengineering, Guangdong Academy of Sciences, Guangzhou 510316, China

ARTICLE INFO

Keywords:
Clay nanotubes
Polypyrrole
Cathode
Interfaces
Sodium ion battery

ABSTRACT

It is a practical challenge to find a cathode material for sodium ion batteries (SIBs) with high capacity and low cost. Here, conductive halloysite nanotubes (Hal) were synthesized by wrapping a layer of polypyrrole (PPy) via in situ polymerization as a potential cathode material for SIBs. By functionalization with PPy, the zeta potential of Hal changed from −28.5 mV to +30.1 mV, which showed excellent aqueous dispersion stability. HR-TEM and XPS results also demonstrated that a continuous conductive layer was formed around the tubes. By virtue of the good electrical conductivity and special tubular structure of Hal@PPy, it was applied as cathode for sodium ion battery. The Hal@PPy electrode could maintain a capacity of 126 mAh g^{-1} after 280 cycles at current density of 200 mA g^{-1}, which suggested a high potential in energy storage fields.

1. Introduction

Sodium ion batteries (SIBs), as one of the renewable energy-storage systems, are promising to alleviate the growing concerns on environmental pollution and energy crisis (Hwang et al., 2017; Mishra et al., 2020; Pu et al., 2019). SIBs exhibit benefits of abundance and low cost of sodium resource, environmentally friendly and similar reaction characteristics with lithium ion batteries. In recent years, lots of cathode materials with high output voltage and high capacity have been developed for SIBs, such as high-voltage layered Na_xMO_2 ($0 < x \leq 1$, M represents transitional metal), Na-rich materials $Na_2M'O_3$ ($M' = Ir, Ru, Sn$, etc.), high-voltage polyanion compounds (phosphates, fluorophosphates, polyanionic compounds, etc. (Liu et al., 2020; You and Manthiram, 2018; Zhao et al., 2012; Zhuang et al., 2020).), hexacyanoferrate (Zhou et al., 2020), prussian blue and its analogues (Wan et al., 2020). However, the large volume expansion of the electrode material during charging and discharging will cause serious deterioration in battery performance due to the larger ion radius of Na^+ (1.02 Å) than Li^+ (0.76 Å). Hence, the cycling stability and charging rate performance of the cathode materials can hardly meet the high requirement, which limits the further development of SIBs. In addition, the high-cost and complicated construction process of electrode materials largely restrict their commercial application (Mishra et al., 2020; Wang et al., 2020; Zheng et al., 2020). Therefore, it is of vital importance to explore the novel cathode materials with superior performance and low cost for SIBs.

Recently, redox-active polymers, such as polyimides, polyquinones, Schiff based polymers and conductive polymers, have been employed as the alternative cathode materials for SIBs, which possess high capacity, low cost, structural diversity, and flexible ionic channels (Baumgartner et al., 2014; Fernández et al., 2018; Sun et al., 2016). For instance, polyquinone and imide-quinone copolymer as cathodes for SIBs exhibited high capacity of 138 mAh g^{-1} and 165 mAh^{-1} g^{-1}, respectively (Deng et al., 2013; Wu et al., 2016; Xu et al., 2015). Among various conductive polymers, polypyrrole (PPy) has been widely applied in SIBs, because of p-doping/dedoping mechanism of anions and high electrical conductivity (Cao et al., 2019; Zhao et al., 2020; Zhou et al., 2013). PPy owns potentially high capacity and flexible ionic channel as electrode materials, which demonstrate high electrical conductivity (10–100 s cm^{-1}). In addition, PPy itself can undergo a fast redox reaction to store charge (Zhou et al., 2013). However, the low surface area, high dissolubility of PPy in electrolytes, and side reaction in eater-based electrolyte during cycling usually led to poor long cycle stability and low rate performances, which made it difficult to meet the actual requirement of the existing SIBs (Su et al., 2015; Zhu et al., 2013). Therefore, it is urgent to improve these aspects of PPy as candidate for the cathode

* Corresponding authors.
E-mail addresses: lihongyan@jnu.edu.cn (H. Li), liumx@jnu.edu.cn (M. Liu).
[1] These authors contributed equally to this work.

https://doi.org/10.1016/j.clay.2021.106265
Received 7 June 2021; Received in revised form 7 August 2021; Accepted 18 August 2021

materials.

In the past decades, as a natural clay mineral with one-dimension structure, halloysite nanotubes (Hal) attract more and more attentions due to their unique structure and high performance (Cavallaro et al., 2018; Du et al., 2010; Shchukin et al., 2005). Hal primarily exists in the form of a hollow tubular structure, and its chemical formula is $Al_2Si_2O_5(OH)_4{\cdot}nH_2O$ (Lvov et al., 2008). The length, inner diameter, and outer diameter of Hal range from 100 to 1500 nm, 15–30 nm, and 50–70 nm, respectively. Interestingly, the inner surfaces of Hal are consist of Si—O—Si groups and the external surfaces are composed of Al—OH groups (Joussein et al., 2005). Hal possess many merits such as easy chemical modification, abundant pore structure, large surface area, high aspect ratio, high strength, good dispersibility, satisfied biocompatibility, and low cost, so Hal are widely applied in different fields (De Silva et al., 2018; Du et al., 2008; Huang et al., 2017; Hughes and King, 2010; Liu and Liu, 2017; Lu et al., 2011; Wu et al., 2019; Zhou et al., 2016). Generally, Hal can be utilized directly or through surface functionalization to obtain a cathode material (Panchal et al., 2018; Shinde et al., 2020; Vergaro et al., 2010). The advantages of Hal mainly include abundantly available with low cost, special 1D tubular structure, and convenience of warpping of conductive polymer layers (Abdullayev et al., 2012; Pei et al., 2020; Wang et al., 2019; Wu et al., 2019; Zhang et al., 2021). For example, Miller et al. prepared solid polymer electrolytes (SPEs) film using Hal together with lithium bis(trifluoromethanesulfonyl)imide and polyethylene oxide. This material shows high ionic conductivity of 1.11×10^{-4} S/cm at 25 °C, and 2.14×10^{-3} S/cm at 100 °C, so it owns wide usage temperature range (25-100 °C) and long cycle performance (Lin et al., 2017). Also, self-assembled carbon microparticles (PCMs) can be constructed using Hal as a template. PCMs behave exceptional ionic and electronic conductivity, while they display a high reversible specific capacity even after 300 cycles and superior rate performance (Subramaniyam et al., 2017). In our previous research, a series of functionalized Hal was prepared by grafting different polymers and silanes (Wu et al., 2019). In addition, the researches of Hal and PPy have been developed for the past decade, for example, a PPy-coated Hal nanocomposite was prepared, which can be applied to the adsorption of Cr(VI) (Ballav et al., 2014). Yang et al. synthesized Hal/PPy nanocomposites with coaxial tubular morphology as electrode materials for supercapacitors, which suggested its potential application in electrode materials (Yang et al., 2010). Considering the good conductivity of PPy, excellent dispersion and load capacity of Hal, the combination of Hal and PPy was supposed, which could have potential in the electrode and battery fields.

Here, in situ polymerization of pyrrole is conducted on the surface of Hal to synthesize Hal@PPy. Siloxane and hydroxyl groups on the surface of Hal provide active sites for polymerization of the pyrroles (Yang et al., 2010). After functionalized with PPy layer, Hal@PPy composite shows excellent dispersity in aqueous systems, which can be attributed to the rich surface charge. Then, Hal@PPy composite material was applied to SIBs as a cathode electrode. It was found that Hal@PPy exhibited a high reversible capacity of 126 mAh g^{-1} at a current density of 200 mA g^{-1} and outstanding cycle stability. Remarkably, Hal@PPy cathode exhibits a high performance compared with state of the art in performance of cathode materials for SIBs, for instance, $Na_2Fe_2(SO_4)_3$ (Chen et al., 2018), $Na_{0.6}Cr_{0.6}Ti_{0.4}O_2$(Wang et al., 2015) and $Na_2MnP_2O_7$ (Li et al., 2019).

2. Experiment

2.1. Material

Hal powder with high-purity was supplied by Guangzhou Runwo Materials Technology Co., Ltd., China. Pyrrole was obtained from Sigma-Aldrich. Ferric chloride ($FeCl_3$) was obtained from Aladdin biochemical technology Ltd., China. Ultra-pure water was used directly from Milli-Q Integral Water Purification System. All the chemicals were used directly without further purification.

2.2. Synthesis of Hal@PPy

Hal@PPy was synthesized according to the previous work with slight modification (Liu and Liu, 2017). Firstly, 4 g of Hal powder was added in 400 mL of deionized water and dispersed uniformly by ultrasonic treatment for 30 min. Afterwards, 4 mL of pyrrole was added and stirred in ice water bath for 1 h. 8 g of $FeCl_3{\cdot}6H_2O$ was injected into the dispersion as a catalyst and the polymerization reaction was performed for 4 h to form a continuous conductive layer on the surface of Hal. The obtained Hal@PPy dispersion was centrifuged and washed using distilled water for three times. Finally, Hal@PPy powder was obtained by freeze drying method at -80 °C. The synthesis process of Hal@PPy was schematically shown in Fig. 1A.

2.3. Characterization

2.3.1. Transmission electron microscopy (TEM)

A drop of 0.05 wt% aqueous dispersion of Hal and Hal@PPy were used to perform the morphology observation by TEM machine (JEOL 2100F, JEOL Ltd., Japan). The elements mapping (C, N, O, Al, Si) was conducted using the same machine.

2.3.2. Scanning electron microscope (SEM)

The morphology and dispersion of Hal and Hal@PPy were characterized by SEM (Zeiss Sigma 500) at 10 kV. The samples were coated with 0.5 nm gold by a sputter coater (SBC-12, China) at 20 mA for 1 min. The working distance was 4.1–4.6 mm.

2.3.3. Fourier transform infrared spectroscopy (FTIR)

A FTIR spectrometer (PerkinElmer, UATR Two) was employed to measure the FTIR spectrum of Hal and Hal@PPy using attenuated total reflection (ATR) model and the scan range was taken from 4000 to 400 cm^{-1}.

2.3.4. X-ray diffraction (XRD)

A diffractometer (Rigaku, Miniflex 600, Cu Kα, Japan) was implemented to detect the XRD pattern of Hal and Hal@PPy at accelerating voltage of 40 kV and current of 40 mA. The scanning range was 5-70° at a scanning speed of 10°/min.

2.3.5. Thermogravimetric analyzer (TGA)

The TGA curves of Hal and Hal@PPy were measured using a TGA instrument (TGA2, METTLER TOLEDO Co. Ltd., Switzerland) at a nitrogen flow rate of 50 mL/min from 50 to 800 °C at a heating rate of 10 °C/min.

2.3.6. Zeta potential and particle size analysis

Zeta potential and hydrodynamic radius measurement of Hal and Hal@PPy dispersion were conducted on Zetasizer Nano ZS (Malvern Instrument Co., U.K.) with a concentration of 0.05 wt%.

2.3.7. X-ray photoelectron spectrum (XPS)

The element analysis was carried out by a XPS machine (ESCALAB250Xi, Thermo Fisher Scientific Ltd., USA). The atoms of C, N, O, Al and Si of Hal and Hal@PPy were tested.

2.4. Fabrication of sodium ion battery cathode

The as-prepared Hal@PPy material, acetylene black, and poly (vinylidene difluoride) (PVDF) (mass ratio of 75:15:15) were mixed into a homogeneous slurry in *N*-methyl-2-pyrrolidone. Then the obtained slurry was cast onto a current collector of Al foil using the doctor blade technique. 1 mol/L of $NaPF_6$ in diethylene glycol dimethyl ether (1:1 by volume) was applied as electrolyte. The glass fiber from Whatman was

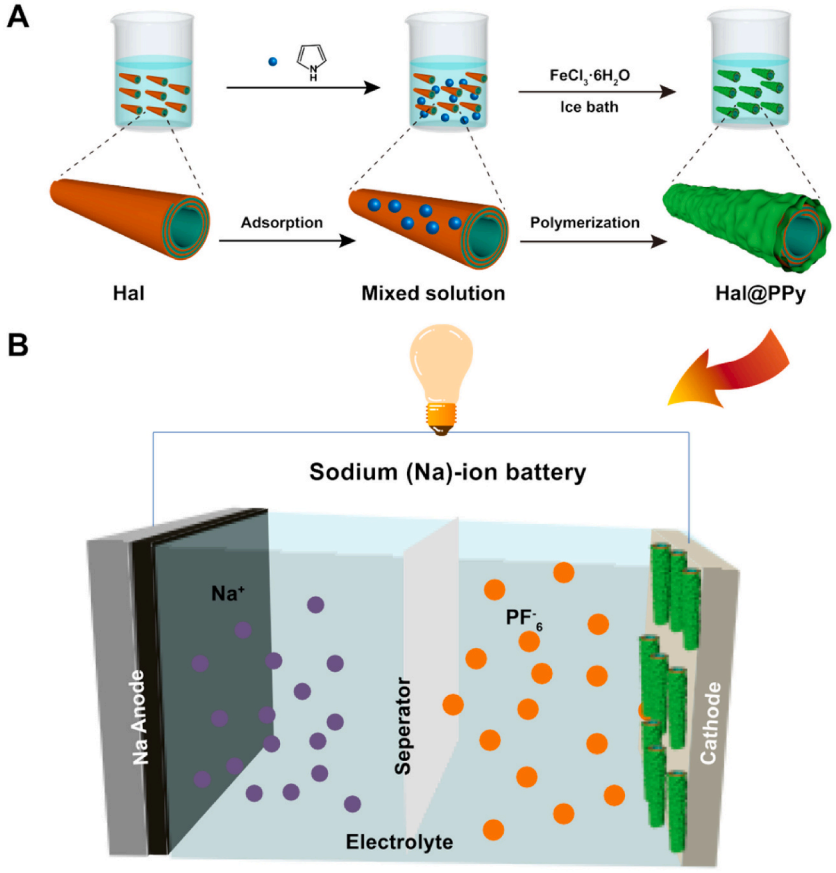

Fig. 1. (A) Schematic illustration for the synthesis of Hal@PPy. (B) Schematic of SIBs assembled with Hal@PPy cathode.

used as the separator. The cells were assembled in an Ar-filled glove box with moisture and oxygen content of less than 0.1 ppm. The pure sodium metal foil was used as counter electrode. The application of Hal@PPy as cathode materials in SIBs was shown in Fig. 1B.

2.5. Electrochemical characterization

Cyclic voltammetry measurements were carried out at different scan rates on a CHI760 Electrochemical Workstation at room temperature. Electrochemical impedance measurements (EIS) were tested range from 0.05 Hz to 100 kHz. LAND-CT2001A battery-testing instruments were used to operate galvanostatic charge and discharge process tests at room temperature under different current densities within a voltage range of 1.3–3.6 V.

3. Results and discussion

3.1. Synthesis and basic characterization

Hal owns rich negatively charged outer surfaces, so they can be properly dispersed in water. This high dispersity is applied to the substrate for loading PPy through in situ chemical oxidation polymerization of pyrrole (Fig. 1A). As expected, PPy was covered on the surface of Hal and a continuous conductive layer was formed around the tubes. The color of Hal is white, while Hal@PPy turns to black totally.

Hal@PPy can be readily dispersed in water and keep outstanding stability for 24 h (Fig. 2A-D). FTIR spectra of Hal and Hal@PPy were investigated and showed in Fig. 2E. The characteristic absorption peaks of Hal appear at 3697 and 3624 cm^{-1}, which are assigned to the O—H stretching vibration of inner-surface hydroxyl groups and inner hydroxyl groups, respectively (Madejová, 2003). As for Hal@PPy, apart from two weak peaks attributed to the hydroxyl groups of Hal, there were some new absorption peaks. For instance, the peaks at 1546 and 1455 cm^{-1} are assigned to the stretching vibration of pyrrole ring, and the peaks at 1301 and 1162 cm^{-1} were attributed to the deforming vibration of C—H (together with N—H) and stretching vibration of C—N, respectively (Wu et al., 2008; Zhou et al., 2015). These results suggest that pyrrole is successfully polymerized on the surfaces of Hal. In the XRD patterns of Hal and Hal@PPy (Fig. 2F), the peak of 2θ at 12.3° (d_{001} = 7.2 Å) corresponded to the first-order basal reflection of (001) plane (Brindley and Goodyear, 1984). As special characteristic of tubular Hal, a sharp peak of 2θ at 20.1° (d_{020} = 4.5 Å) was also identified. An additional peak was observed at 2θ of 24.8°, which could be attributed to the d_{002} plane with a basal spacing of 3.6 Å. The diffraction peaks of 2θ at 35.6°, 36.2° and 28.5° corresponded to (130), (131) and (003) crystalline plane, respectively. These XRD peaks of Hal and Hal@PPy showed similar characteristic diffractions of Hal, which demonstrated that the crystal structure is maintained after wrapping PPy. The characteristic reflection at 18.2° assigned to Fe_3O_4 and reflection at 30.2° assigned to FeO, $KAlSi_3O_8$ (feldspar) and $KAl_3(SO_4)_2(OH)_6$ (alunite) was found in XRD pattern, due to the existence of impurity in these two samples (Ece and Schroeder, 2007). TGA curves of Hal and Hal@PPy are displayed in Fig. 2G. The residual of Hal@PPy was less than that of Hal, which is caused by decomposition of PPy coated on the surface of Hal. During the heating process from 30 to 800 °C, the TGA curves show that the remaining mass of Hal and Hal@PPy is 80.85% and 61.37%, respectively. The mass loss of Hal is mainly attributed to the loss of adsorbed water and hydroxyl dehydration. As for Hal@PPy, apart from the evaporation of water and dehydration of hydroxyl, there was the decomposition of PPy attached on the surfaces of Hal. Therefore, the content of Hal@PPy can be calculated according to difference of the remaining mass of Hal and Hal@PPy, and the result shows the loading of

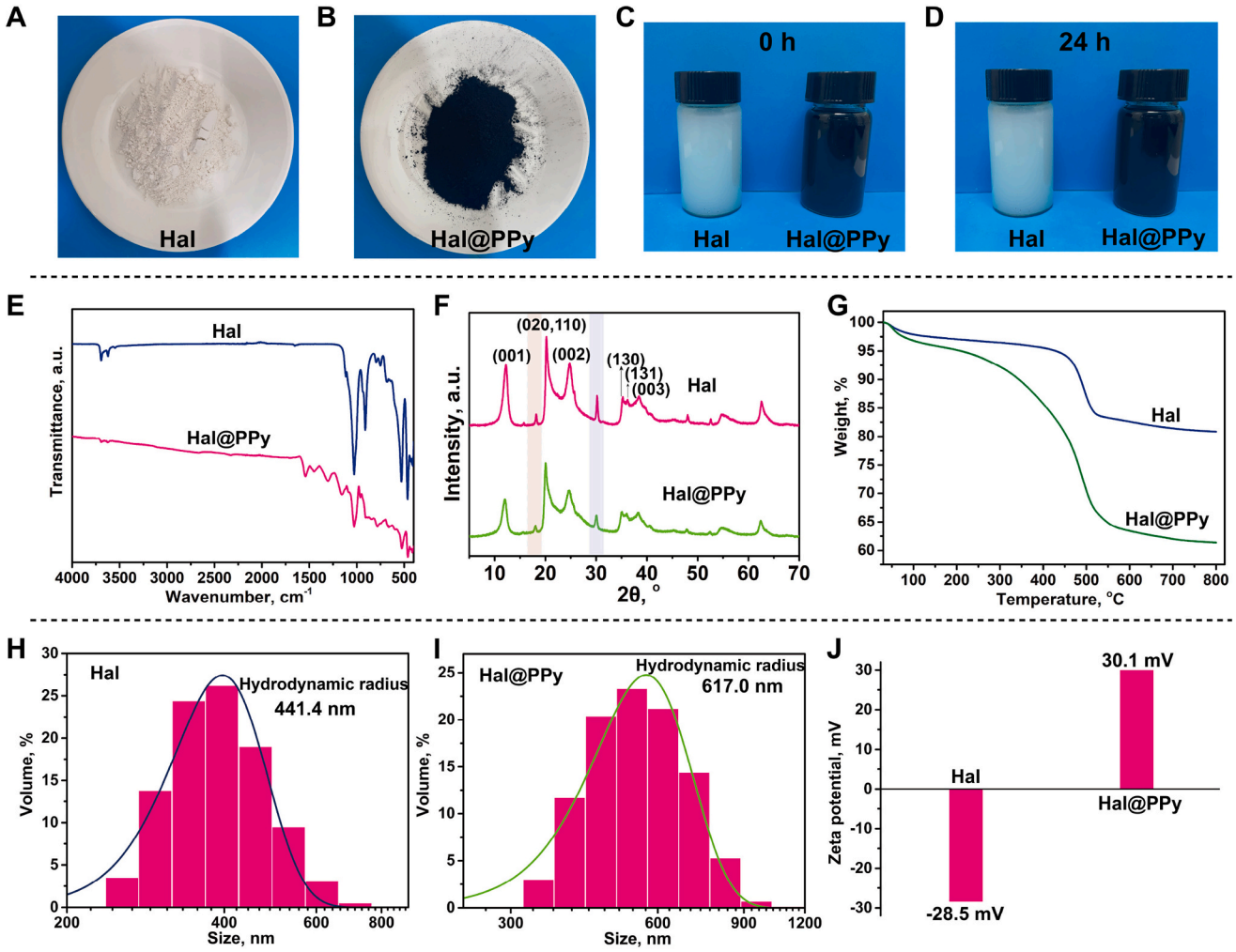

Fig. 2. (A, B, C and D) Photos of Hal, Hal@PPy powders and dispersions. (E) IR, (F) XRD and (G) thermogravimetric curves of Hal and Hal@PPy. Hydrodynamic radius distribution of (H) Hal and (I) Hal@PPy dispersions. (J) Zeta potential of Hal and Hal@PPy dispersions.

PPy on Hal is 19.48%. The hydrodynamic radius of Hal@PPy is 617.0 nm which is higher than that of Hal (441.4 nm) (Fig. 2H and I). The increment can be attributed to the wrapping of PPy layer on the surfaces of Hal, which is consistent with XRD results. The zeta potential value of Hal is −28.5 mV (Fig. 2 J), and the zeta potential of Hal@PPy changed to +30.1 mV after coated with PPy. The increase of zeta potential of Hal@PPy is caused by the coating of positively charged PPy. The PPy with positively charge interacts preferentially with the large area of the Hal external surface with negative charge, which causes the variation of zeta potential value by neutralization effect (Lazzara et al., 2018). According to the DLVO theory and zeta potential data, the increase of net surface charge generates an improvement of the Hal stability in water because of the enhancement of the electrostatic repulsion (Cavallaro et al., 2020). As a result, Hal@PPy is able to be dispersed in water and kept stable.

3.2. Analysis of morphology

As displayed in Fig. 3A and B, the surface morphology of Hal and Hal@PPy was different. It can be observed in SEM images that Hal demonstrate a high aspect ratio and their tube walls are smooth and sharp. After polymerization of pyrrole, it is obvious that the external surfaces of Hal@PPy are covered with a layer of polymer and their surfaces get rough and thick. This also suggests that PPy was coated on the surface of Hal successfully and the continuous conductive layer was formed. The morphology of Hal and Hal@PPy was also analyzed by TEM and elemental mapping. Hal shows hollow tubular-like structure while Hal@PPy shows different morphology. It is clear that there is a layer covered on the outer surface of tube and thickness of the layer is about 8.69 ± 6.34 nm. This further confirms that PPy was coated on the surface of Hal uniformly. Subsequently, the elemental mapping (C, N, O, Al and Si) of Hal and Hal@PPy was conducted. There are very small amounts of elements of carbon and nitrogen in Hal. By contrast, the tube in Hal@PPy is wrapped with a polymer layer which contains elements of C and N. These results also illustrate that PPy was synthesized at the surface of Hal.

3.3. XPS analysis

To further confirm the chemical states and banding configuration of Hal and Hal@PPy, the XPS measurement was carried out. The atomic percentage of Hal and Hal@PPy is listed in Table 1. The survey of XPS spectra of Hal@PPy and Hal are displayed separately in Fig. 4A and Fig. 5A. In contrast, it is obvious that the element of N and C present in Hal@PPy and the contents of C and N for Hal@PPy are increased. Afterwards, the Al 2p and Si 2p binding energy of Hal@PPy slightly shift to lower binding energy compared to the Hal (Fig. 5B and C). This phenomenon could be attributed to electron clouds from exterior of PPy to the interior of Hal, indicating the formation of strong synergistic coupling effect of Hal and PPy. In Fig. 4B, the C 1 s spectrum is separated

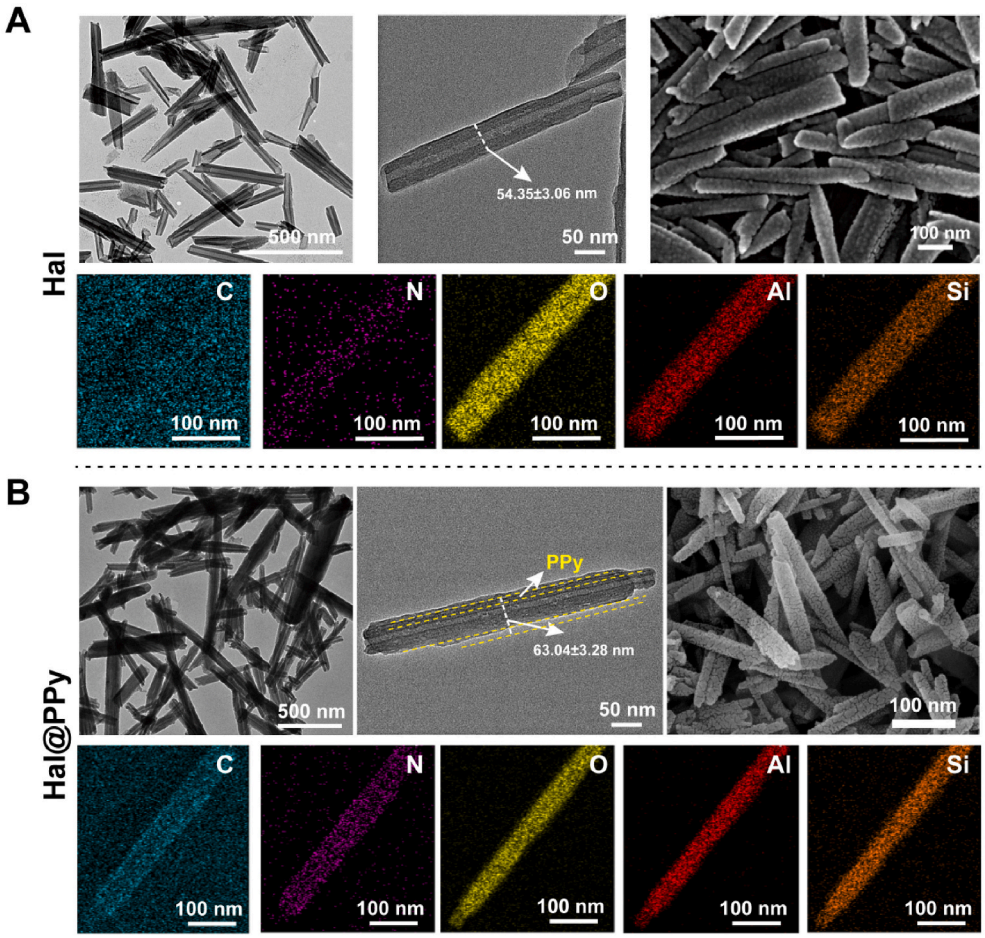

Fig. 3. TEM, SEM images and elemental mapping of (A) Hal and (B) Hal@PPy.

Table 1
Atomic percentage (%) of Hal and Hal@PPy by XPS measurement.

Sample	C 1s	N 1s	O 1s	Cl 2p	Al 2p	Si 2p
Hal@PPy	59.76 ± 0.27	10.20 ± 2.31	20.44 ± 4.19	4.72 ± 0.67	4.23 ± 0.04	3.00 ± 0.55
Hal	13.99 ± 0.87	/	55.42 ± 0.71	0.67 ± 0.28	14.00 ± 0.18	16.27 ± 0.26

into three peaks at 284.1 eV, 285.0 eV and 286.4 eV, which were corresponding to the C═C, C—C and C—N bonds of PPy, respectively. Moreover, the spectra of N 1 s for Hal@PPy can be divided into two obvious peaks located at 399.7 eV and 401.2 eV (Fig. 4C) (Xiong et al., 2013). In addition, the O 1 s core-level spectrum of Hal and Hal@PPy can be deconvoluted to two peaks at 532.2 eV (Al—O) and 532.9 eV (Si—O) (Fig. 4D and E) (Yang et al., 2020). The intensities of Al—O and Si—O peaks decreased in Hal@PPy. These results further confirm that PPy has been synthesized around of the tubes successfully.

3.4. Electrochemical performance

Due to its good electrical conductivity and special tubular structure, Hal@PPy can be used as a potential electrode material in energy storage devices. In addition, the electroactive conductive polymer (PPy) has potentially high redox capacity and flexible host matrixes for p-doping/dedoping reaction of anions, irrespective of the nature of cations, thus seeming to be a suitable candidate for the cathode materials of SIBs. Therefore, Hal@PPy and sodium metal were assembled into battery as the cathode and the counter electrode, respectively. The electrochemical properties of Hal@PPy based SIBs were characterized and showed in Fig. 6. Typically, cyclic voltammetry (CV) is employed to get further insight into sodium storage behaviors. In Fig. 6A, it can be seen that the CV curves of Hal@PPy based sodium ion batteries at different scan rates of 1, 2, 3 and 5 mV s^{-1} (Potential window: 1.3–3.6 V). Taking the curve of 1 mV s^{-1} as example, the two oxidation peaks and two reduction peaks were observed at 2.8/3.2 V and 1.7/2.0 V, respectively. Although the positions of the oxidation peak and the reduction peak shift slightly after the scan rate increasing, the shape of the CV curves remain unchanged. It means that Hal@PPy composite material has excellent stability and rate performance. According to these phenomenon and analysis, the redox reaction in Hal@PPy based sodium ion batteries can be attributed to the reversible insertion/extraction of the electrolyte anions of PF^-_6. Simultaneously, the charge and discharge mechanism of the Hal@PPy cathode was presented in the following equation:

$$\text{Cathode}: \text{Hal@PPy} + PF^-_6 \leftrightarrow \text{Hal@PPy}^+ \, PF^-_6 + e \quad (1)$$

$$\text{Anode}: Na^+ + e \leftrightarrow Na \quad (2)$$

$$\text{Overall reaction}: \text{Hal@PPy} + PF^-_6 + Na^+ \leftrightarrow \text{Hal@PPy}^+ \, PF^-_6 + Na \quad (3)$$

The electrochemical mechanism of PPy as a SIBs cathode material is based on reversible doping/dedoping of anions (PF_6^-). The Hal with hydroxyl groups is easy to form hydrogen bond with fluorine atom in PF_6^-. These hydroxyl groups can reduce the pairing of sodium salt ion and enhance the dissociation degree of free ions and carriers, which improved ion transfer in electrolyte. Besides, Hal possesses positively charged internal and negatively charged external surface. This unique property can enrich active site and ion storage. The internal lumen with

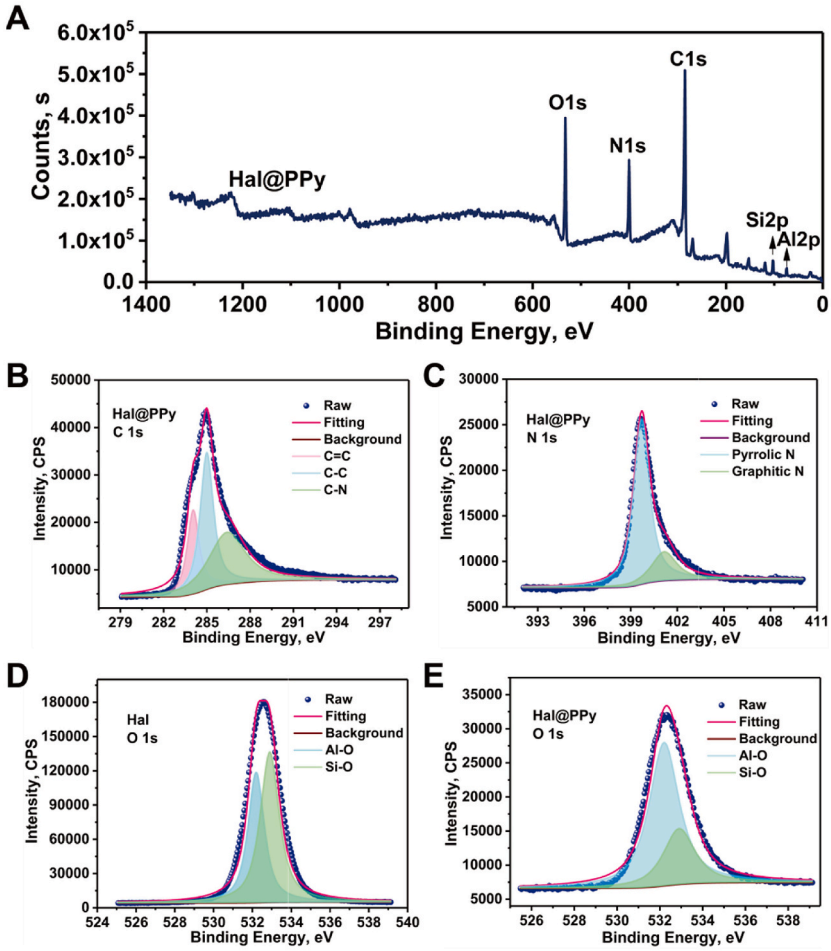

Fig. 4. The survey of XPS spectra of (A) Hal@PPy. High-resolution scanning of (B) carbon and (C) nitrogen for Hal@PPy. High-resolution scanning of oxygen for (D) Hal and (E) Hal@PPy.

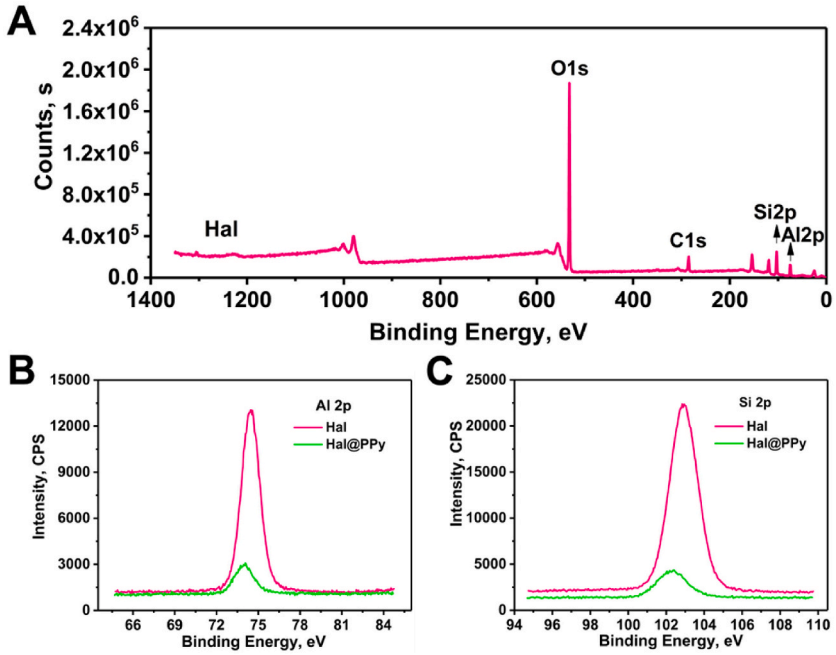

Fig. 5. The survey of XPS spectra of (A) Hal. High-resolution scanning of (B) Al and (C) Si for Hal and Hal@PPy.

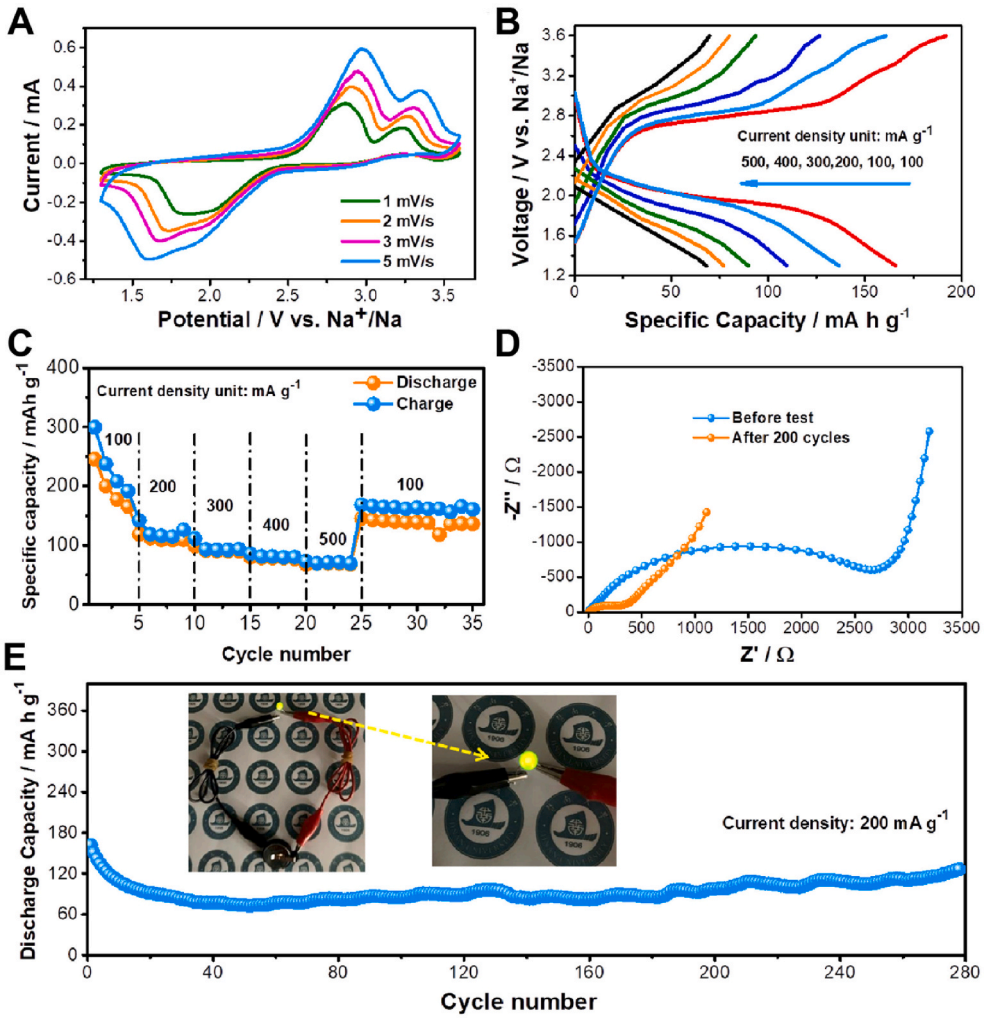

Fig. 6. (A) CV curves of Hal@PPy at different scan rates (1, 2, 3, 5 mV s^{-1}). (B) Galvanostatic charge/discharge curves at different current densities (100, 200, 300, 400, 500 mA g^{-1}). (C) Rate capabilities of Hal@PPy based cell at different current densities (100, 200, 300, 400, 500 mA g^{-1}). (D) Comparison of EIS curves between before cell test with after cell test. (E) The cycling stability of Hal@PPy based cell at the current density of 200 mA g^{-1}. The inset photograph of (E) showing Hal@PPy based cell lighted green LED. (For interpretation of the references to color in this figure legend, the reader is referred to the web version of this article.)

positive charge is easy to absorb PF_6^- ion by electrostatic adherence. Also, the outer surface with negative charge can enhance adsorption of Na^+ by electrostatic adherence.

Fig. 6B shows the charge/discharge curves against the specific capacity and voltage. The plateau in the charge/discharge curves and the position of the redox peak in the CV curves can be consistent. The rate capability of the Hal@PPy cathode is demonstrated in Fig. 6C, which shown the reversible capacity of the electrode was 164, 99, 80, 68 and 67 mAh g^{-1} at the current density of 100, 200, 300, 400 and 500 mA g^{-1}, respectively. In addition, the electrode was able to maintain a reversible capacity of 147 mAh g^{-1} at the current density of 100 mA g^{-1} after cycling at high current densities. This result suggests that the Hal@PPy electrode could provide more electrochemical active sites on the surface of PPy. The hollow tubular structure would promote the ion diffusion, resulting in improving electrochemical performance. At the same time, PPy was functionalized on the surface of Hal, which can further prevent aggregation and expose more active sites. The Hal@PPy composite cathode exhibited a high performance compared with highly developed performance of cathode materials for SIBs, for instance, $Na_2Fe_2(SO_4)_3$ (100 mAh g^{-1} at current density less than 30 mA g^{-1}) and $Na_{0.6}Cr_{0.6}Ti_{0.4}O_2$ (<75 mAh g^{-1} at 7.6 mA g^{-1}) and $Na_2MnP_2O_7$ (90 mAh g^{-1} at a current density less than 10 mA g^{-1}). The self-activation process of materials can help to further reduce the internal diffusion resistance for the batteries. Hence, the electrochemical impedance spectroscopy (EIS) was performed to track the diffusion resistance after certain cycles of batteries. As shown in Fig. 6D, the two Nyquist plots are featured by two well-defined regions, a semicircle in the high-frequency region and a straight line in the low-frequency region. It is found that the charge transfer resistance decreases from 2500 Ω (before test) to 300 Ω (200th cycle) at a current density of 200 mA g^{-1}. The decrease of resistance during cycling progresses further and displayed the excellent stability of Hal@PPy in electrochemical process as well as the self-activation process of the material. Notably, the Hal@PPy cathode maintained its capacity of 126 mAh g^{-1} after 280 cycles at a high current density of 200 mA g^{-1} (Fig. 6E). Moreover, in order to further verify the potential of Hal@PPy in SIBs, the Hal@PPy based sodium ion batteries could power a commercial green LED (1.7–2.3 V) for a few minutes (inset of Fig. 6E). This work provides new insights for construction of Hal-based materials for energy storage field.

4. Conclusions

A conductive Hal@PPy composite was constructed using in situ polymerization method. The zeta potential of Hal transferred from −28.5 mV to +30.1 mV after functionalized with PPy, which demonstrates that conductive PPy layers were formed on Hal. The composite shows excellent dispersion ability and stability in water. When worked as cathode of SIBs, the Hal@PPy electrode exhibited a capacity of 126 mAh g^{-1} after 280 cycles at a high current density of 200 mA g^{-1}. The Hal@PPy based electrodes exhibited a superior performance compared with advanced cathode materials for SIBs. In particular, the in-situ polymerization method described here is a facile and easy way to functionalize Hal, which provides a new method to create cathode materials for energy storage applications.

Credit author statements

Xiang Cao and Yingjuan Sun carried out the experiment and wrote the manuscript. Yongrong Sun assisted on the materials synthesis experiment and revised the manuscript. Hongyan Li and Mingxian Liu supervised the project and took the lead in writing the manuscript. Dong Xie contributed to the interpretation of the results and gave the advice on the manuscript.

Declaration of Competing Interest

The authors declare that they have no known competing financial interests or personal relationships that could have appeared to influence the work reported in this paper.

Acknowledgements

This work was financially supported by the National Natural Science Foundation of China (52073121), Natural Science Foundation of Guangdong Province (2019A1515011509), Science and Technology Planning Project of Guangdong Province (2019A050513004), Science and Technology Program of Guangzhou, China (202102010117) and the Fundamental Research Funds for the Central Universities (21619102). H. Li also acknowledges the support from the Start-up Funding of Jinan University (88016105 and 55800001), the Discipline Construction Outstanding Young Backbone Project (12819023), Guangdong Basic and Applied Basic Research Foundation (2020A1515110611 and 2021A1515010362), and the Fundamental Research Funds for the Central Universities (21620317).

References

Abdullayev, E., Joshi, A., Wei, W.B., Zhao, Y.F., Lvov, Y., 2012. Enlargement of halloysite clay nanotube lumen by selective etching of aluminum oxide. ACS Nano 6, 7216–7226.

Ballav, N., Choi, H.J., Mishra, S.B., Maity, A., 2014. Polypyrrole-coated halloysite nanotube clay nanocomposite: synthesis, characterization and Cr (VI) adsorption behaviour. Appl. Clay Sci. 102, 60–70.

Baumgartner, B., Bojdys, M.J., Unterlass, M.M., 2014. Geomimetics for green polymer synthesis: highly ordered polyimides via hydrothermal techniques. Polym. Chem. 5, 3771–3776.

Brindley, W., Goodyear, J., 1984. X-ray studies of halloysite and metahalloysite: part II. The transition of halloysite to metahalloysite in relation to relative humidity. Mineral. Magaz. J. Mineral. Soc. 28, 407–422.

Cao, L., Zhang, B., Ou, X., Wang, C., Peng, C., Zhang, J., 2019. Synergistical coupling interconnected ZnS/SnS_2 nanoboxes with polypyrrole-derived N/S dual-doped carbon for boosting high-performance sodium storage. Small 15, 1804861.

Cavallaro, G., Lazzara, G., Milioto, S., Parisi, F., Evtugyn, V., Rozhina, E., Fakhrullin, R., 2018. Nanohydrogel formation within the halloysite lumen for triggered and sustained release. ACS Appl. Mater. Interfaces 10, 8265–8273.

Cavallaro, G., Milioto, S., Konnova, S.A., Fakhrullina, G., Lvov, Y., 2020. Halloysite/keratin nanocomposite for human hair photoprotection coating. ACS Appl. Mater. Interfaces 12, 24348–24362.

Chen, M., Cortie, D., Hu, Z., Jin, H., Wang, S., Gu, Q., Hua, W., Wang, E., Lai, W., Chen, L., 2018. A novel graphene oxide wrapped $Na_2Fe_2(SO_4)_3$/C cathode composite for long life and high energy density sodium-ion batteries. Adv. Energy Mater. 8, 1800944.

De Silva, R.T., Dissanayake, R.K., Mantilaka, M.P.G., Wijesinghe, W.S.L., Kaleel, S.S., Premachandra, T.N., Weerasinghe, L., Amaratunga, G.A., de Silva, K.N., 2018. Drug-loaded halloysite nanotube-reinforced electrospun alginate-based nanofibrous scaffolds with sustained antimicrobial protection. ACS Appl. Mater. Interfaces 10, 33913–33922.

Deng, W., Liang, X., Wu, X., Qian, J., Cao, Y., Ai, X., Feng, J., Yang, H., 2013. A low cost, all-organic Na-ion battery based on polymeric cathode and anode. Sci. Rep. 3, 1–6.

Du, M., Guo, B., Lei, Y., Liu, M., Jia, D., 2008. Carboxylated butadiene–styrene rubber/halloysite nanotube nanocomposites: interfacial interaction and performance. Polymer 49, 4871–4876.

Du, M., Guo, B., Jia, D., 2010. Newly emerging applications of halloysite nanotubes: a review. Polym. Int. 59, 574–582.

Ece, O.I., Schroeder, P.A., 2007. Clay mineralogy and chemistry of halloysite and alunite deposits in the Turplu area, Balikesir, Turkey. Clay Clay Miner. 55, 18–35.

Fernández, N., Sánchez-Fontecoba, P., Castillo-Martínez, E., Carretero-González, J., Rojo, T., Armand, M., 2018. Polymeric redox-active electrodes for sodium-ion batteries. ChemSusChem 11, 311–319.

Huang, B., Liu, M., Zhou, C., 2017. Cellulose–halloysite nanotube composite hydrogels for curcumin delivery. Cellulose 24, 2861–2875.

Hughes, A.D., King, M.R., 2010. Use of naturally occurring halloysite nanotubes for enhanced capture of flowing cells. Langmuir 26, 12155–12164.

Hwang, J.-Y., Myung, S.-T., Sun, Y.-K., 2017. Sodium-ion batteries: present and future. Chem. Soc. Rev. 46, 3529–3614.

Joussein, E., Petit, S., Churchman, J., Theng, B., Righi, D., Delvaux, B., 2005. Halloysite clay minerals—a review. Clay Miner. 40, 383–426.

Lazzara, G., Cavallaro, G., Panchal, A., Fakhrullin, R., Stavitskaya, A., Vinokurov, V., Lvov, Y., 2018. An assembly of organic-inorganic composites using halloysite clay nanotubes. Curr. Opin. Colloid Interface Sci. 35, 42–50.

Li, H., Chen, X., Jin, T., Bao, W., Zhang, Z., Jiao, L., 2019. Robust graphene layer modified $Na_2MnP_2O_7$ as a durable high-rate and high energy cathode for Na-ion batteries. Energy Stor. Mater. 16, 383–390.

Lin, Y., Wang, X., Liu, J., Miller, J.D., 2017. Natural halloysite nano-clay electrolyte for advanced all-solid-state lithium-sulfur batteries. Nano Energy 31, 478–485.

Liu, Y., Liu, M., 2017. Conductive carboxylated styrene butadiene rubber composites by incorporation of polypyrrole-wrapped halloysite nanotubes. Compos. Sci. Technol. 143, 56–66.

Liu, S., Cao, X., Zhang, Y., Wang, K., Su, Q., Chen, J., He, Q., Liang, S., Cao, G., Pan, A., 2020. Carbon quantum dot modified $Na_3V_2(PO_4)_2F_3$ as a high-performance cathode material for sodium-ion batteries. J. Mater. Chem. A 8, 18872–18879.

Lu, D., Chen, H., Wu, J., Chan, C.M., 2011. Direct measurements of the Young's modulus of a single halloysite nanotube using a transmission electron microscope with a bending stage. J. Nanosci. Nanotechnol. 11, 7789–7793.

Lvov, Y.M., Shchukin, D.G., Mohwald, H., Price, R.R., 2008. Halloysite clay nanotubes for controlled release of protective agents. ACS Nano 2, 814–820.

Madejová, J., 2003. FTIR techniques in clay mineral studies. Vib. Spectrosc. 31, 1–10.

Mishra, K., Yadav, N., Hashmi, S., 2020. Recent progress in electrode and electrolyte materials for flexible sodium-ion batteries. J. Mater. Chem. A 8, 22507–22543.

Panchal, A., Fakhrullina, G., Fakhrullin, R., Lvov, Y., 2018. Self-assembly of clay nanotubes on hair surface for medical and cosmetic formulations. Nanoscale 10, 18205–18216.

Pei, Y., Wang, Y., Darraf, Y., Chang, A.Y., Zhao, H., Liu, X., Liu, J., Lvov, Y., Wang, S., 2020. Confining sulfur particles in clay nanotubes with improved cathode performance of lithium–sulfur batteries. J. Power Sources 450, 227698.

Pu, X., Wang, H., Zhao, D., Yang, H., Ai, X., Cao, S., Chen, Z., Cao, Y., 2019. Recent progress in rechargeable sodium-ion batteries: toward high-power applications. Small 15, 1805427.

Shchukin, D.G., Sukhorukov, G.B., Price, R.R., Lvov, Y.M., 2005. Halloysite nanotubes as biomimetic nanoreactors. Small 1, 510–513.

Shinde, S., Ghodake, G., Maile, N., Yadav, H., Jagadale, A., Jalak, M., Kadam, A., Ramesh, S., Bathula, C., Kim, D.-Y., 2020. Designing of nanoflakes anchored nanotubes-like $MnCo_2S_4$/halloysite composites for advanced battery like supercapacitor application. Electrochim. Acta 341, 135973.

Su, D., Zhang, J., Dou, S., Wang, G., 2015. Polypyrrole hollow nanospheres: stable cathode materials for sodium-ion batteries. Chem. Commun. 51, 16092–16095.

Subramaniyam, C.M., Srinivasan, N., Tai, Z., Liu, H.K., Goodenough, J.B., Dou, S.X., 2017. Self-assembled porous carbon microparticles derived from halloysite clay as a lithium battery anode. J. Mater. Chem. A 5, 7345–7354.

Sun, T., Li, Z.j., Wang, H.g., Bao, D., Meng, F.l., Zhang, X.b., 2016. A biodegradable polydopamine-derived electrode material for high-capacity and long-life lithium-ion and sodium-ion batteries. Angew. Chem. Int. Ed. 55, 10662–10666.

Vergaro, V., Abdullayev, E., Lvov, Y.M., Zeitoun, A., Cingolani, R., Rinaldi, R., Leporatti, S., 2010. Cytocompatibility and uptake of halloysite clay nanotubes. Biomacromolecules 11, 820–826.

Wan, P., Xie, H., Zhang, N., Zhu, S., Wang, C., Yu, Z., Chu, W., Song, L., Wei, S., 2020. Stepwise hollow prussian blue nanoframes/carbon nanotubes composite film as ultrahigh rate sodium ion cathode. Adv. Funct. Mater. 30, 2002624.

Wang, Y., Xiao, R., Hu, Y.-S., Avdeev, M., Chen, L., 2015. P_2-$Na_{0.6}$ $[Cr_{0.6}Ti_{0.4}]O_2$ cation-disordered electrode for high-rate symmetric rechargeable sodium-ion batteries. Nat. Commun. 6, 6954.

Wang, Y.Y., Wang, X.B., Ye, H.Q., Han, K., 2019. Carbon coated halloysite nanotubes as efficient sulfur host materials for lithium sulfur batteries. Appl. Clay Sci. 179, 105172.

Wang, L., Ni, Y., Hou, X., Chen, L., Li, F., Chen, J., 2020. A two-dimensional metal–organic polymer enabled by robust nickel–nitrogen and hydrogen bonds for exceptional sodium-ion storage. Angew. Chem. Int. Ed. 59, 22126–22131.

Wu, J., Li, Q., Fan, L., Lan, Z., Li, P., Lin, J., Hao, S., 2008. High-performance polypyrrole nanoparticles counter electrode for dye-sensitized solar cells. J. Power Sources 181, 172–176.

Wu, D., Huang, Y., Hu, X., 2016. A sulfurization-based oligomeric sodium salt as a high-performance organic anode for sodium ion batteries. Chem. Commun. 52, 11207–11210.

Wu, F., Pickett, K., Panchal, A., Liu, M.X., Lvov, Y., 2019. Superhydrophobic polyurethane foam coated with polysiloxane-modified clay nanotubes for efficient and recyclable oil absorption. ACS Appl. Mater. Interfaces 11, 25445–25456.

Xiong, B., Zhou, Y., Zhao, Y., Wang, J., Chen, X., O'Hayre, R., Shao, Z., 2013. The use of nitrogen-doped graphene supporting Pt nanoparticles as a catalyst for methanol electrocatalytic oxidation. Carbon 52, 181–192.

Xu, F., Xia, J., Shi, W., 2015. Anthraquinone-based polyimide cathodes for sodium secondary batteries. Electrochem. Commun. 60, 117–120.

Yang, C., Liu, P., Zhao, Y., 2010. Preparation and characterization of coaxial halloysite/polypyrrole tubular nanocomposites for electrochemical energy storage. Electrochim. Acta 55, 6857–6864.

Yang, X., Zhang, Y., Zheng, D., Yue, J., Liu, M., 2020. Nano-biocomposite films fabricated from cellulose fibers and halloysite nanotubes. Appl. Clay Sci. 190, 105565.

You, Y., Manthiram, A., 2018. Progress in high-voltage cathode materials for rechargeable sodium-ion batteries. Adv. Energy Mater. 8, 1701785.
Zhang, Q., Zhang, Y., Liu, S.N., Yang, H.M., 2021. Nitrogen-doped three-dimensional porous carbon anode derived from hard halloysite template for sodium-ion batteries. Appl. Clay Sci. 200, 105916.
Zhao, R., Zhu, L., Cao, Y., Ai, X., Yang, H.X., 2012. An aniline-nitroaniline copolymer as a high capacity cathode for Na-ion batteries. Electrochem. Commun. 21, 36–38.
Zhao, D., Dai, M., Zhao, Y., Liu, H., Liu, Y., Wu, X., 2020. Improving electrocatalytic activities of $FeCo_2O_4$@$FeCo_2S_4$@PPy electrodes by surface/interface regulation. Nano Energy 104715.
Zheng, S., Huang, H., Dong, Y., Wang, S., Zhou, F., Qin, J., Sun, C., Yu, Y., Wu, Z.-S., Bao, X., 2020. Ionogel-based sodium ion micro-batteries with a 3D Na-ion diffusion mechanism enable ultrahigh rate capability. Energy Environ. Sci. 13, 821–829.
Zhou, M., Xiong, Y., Cao, Y., Ai, X., Yang, H., 2013. Electroactive organic anion-doped polypyrrole as a low cost and renewable cathode for sodium-ion batteries. J. Polym. Sci. B Polym. Phys. 51, 114–118.
Zhou, L., Cai, D., He, L., Zhong, N., Yu, M., Zhang, X., Wu, Z., 2015. Fabrication of a high-performance fertilizer to control the loss of water and nutrient using micro/nano networks. ACS Sustain. Chem. Eng. 3, 645–653.
Zhou, X., Wu, L., Yang, J., Tang, J., Xi, L., Wang, B., 2016. Synthesis of nano-sized silicon from natural halloysite clay and its high performance as anode for lithium-ion batteries. J. Power Sources 324, 33–40.
Zhou, A., Cheng, W., Wang, W., Zhao, Q., Xie, J., Zhang, W., Gao, H., Xue, L., Li, J., 2020. Hexacyanoferrate-type prussian blue analogs: principles and advances toward high-performance sodium and potassium ion batteries. Adv. Energy Mater. 2000943.
Zhu, L., Shen, Y., Sun, M., Qian, J., Cao, Y., Ai, X., Yang, H., 2013. Self-doped polypyrrole with ionizable sodium sulfonate as a renewable cathode material for sodium ion batteries. Chem. Commun. 49, 11370–11372.
Zhuang, X., Li, K., Zhang, T.-Y., 2020. Partial sodiation induced laminate structure and high cycling stability of black phosphorous for sodium-ion batteries. Nanoscale 12, 19609–19616.